South African Journal of Chemical Engineering 55 (2026) 368–379

Contents lists available at ScienceDirect

South African Journal of Chemical Engineering

journal homepage: www.elsevier.com/locate/sajce

Adsorptive removal of Carbamazepine from synthetic wastewater using *Moringa oleifera* seed coat

Peace S. Azeh, Monsurat O. Jimoh, Mabafokeng Masitha, Samuel A. Iwarere, Michael O. Daramola *

Sustainable Energy and Environment Research Group, Department of Chemical Engineering, Faculty of Engineering, Built Environment and Information Technology, University of Pretoria, Hatfield Campus, Pretoria 0002, South Africa

ARTICLE INFO

Keywords:
Adsorption
Carbamazepine
Moringa oleifera
Seed coat

ABSTRACT

Biosorption has demonstrated effectiveness in eliminating contaminants of emerging concern (CECs) that lack inclusion in current water quality standards. These pollutants impede progress towards UN Sustainable Development Goals 6 and 14, pertaining to clean water accessibility and marine life preservation. This research investigated the adsorption potential of the persistent pharmaceutical pollutant, carbamazepine, using *Moringa oleifera* (MO) seed coat. This research investigated the adsorption potential of the persistent pharmaceutical pollutant, carbamazepine, using MO seed coat biochar. Acid hydrolysis and subsequent carbonization produced a biochar with superior properties for adsorption as confirmed by FTIR, SEM, EDX, CHNOS, and XRD analyses. The influence of agitation speed (200 rpm, 300 rpm, and 400 rpm), adsorption duration (0 to 180 min), and adsorption temperature (30 °C, 40 °C, and 50 °C) on CBZ removal in synthetic wastewater were studied.

The quadratic regression model obtained from Box Behnken experimental design (BBD) with Response surface methodology (RSM) showed a strong predictive ability with $R^2 = 0.9754$ and adjusted-$R^2 = 0.9015$. Agitation speed significantly influenced the adsorption capacity as evidenced by a p-value of 0.02848. The optimum conditions for CBZ adsorption were 400 rpm, 30 °C, and 2.15 h at which a maximum adsorption capacity of 51.87 mg/g was anticipated. The adsorption behaviour was best described by pseudo-second order kinetics and the Temkin isotherm model. The study confirmed that MO seed coat biochar as a promising green adsorbent for pharmaceutical contaminant removal in wastewater treatment.

1. Introduction

Contaminants of emerging concern (CECs) are pollutants which are typically not removed by conventional water treatment processes due to their chemical composition/structure and aged water and wastewater treatment technology. Carbamazepine (CBZ) is one of such contaminants. CBZ ($C_{15}H_{12}N_2O$) is an anticonvulsant drug and mood stabiliser used for the management of epilepsy and bipolar disorder. Upon ingestion CBZ forms metabolites such as CBZ-epoxide, CBZ-acridan, 2-OH—CBZ and 3-OH—CBZ and CBZ-diol and the unused drug is excreted in urine or faeces. Carbamazepine has a solubility limit of 17.7 mg/L in water at 25 °C and its water partition coefficient $\log K_{ow}$ is 2.45 – these make CBZ practically insoluble in water (Zhang et al., 2008). CBZ has 2 pKa values; pKa = 2.3 and pKa = 13.9. Between these pH values, CBZ is neutrally charged and thus not ionisable (Radjenovic' et al., 2008; Couto et al., 2019).

For these reasons, CBZ cannot be readily removed from water and has been detected in WWTP effluent, surface waters, and ground water. The detection of CBZ in various water sources is concerning because the predicted no-effect concentration (PNEC) for ecotoxicity of CBZ is 25 ng/L (Tran et al., 2018) but several authors have reported much higher detected concentrations. In South Arica, the CBZ concentration in drinking water vary from 325 ng/L (Odendaal et al., 2015) to 500 ng/L (Archer et al., 2017). CBZ detection in groundwater ranges from 9.3 ng/L in Singapore (Tran et al., 2014) to 335 ng/L in Cameroon (Branchet et al., 2019). Its detection limit is even greater in WWTP effluent – 49 ng/L in China (Wu et al., 2015) to ±404.3 ng/L in the USA (Bartlet-Hunt et al., 2009). According to Cunningham et al. (2010) the maximum detection of CBZ was in surface waters in the USA and Europe are 1500 ng/L and 11.581 μg/L, respectively. These concentrations are harmful to aquatic life. Cleuvers (2003) reported that exposure of Lemna minor to CBZ resulted in growth inhibition of the algae – supported by the

* Corresponding author.
E-mail address: michael.daramola@up.ac.za (M.O. Daramola).

https://doi.org/10.1016/j.sajce.2025.11.015
Received 27 December 2024; Received in revised form 3 November 2025; Accepted 19 November 2025
Available online 20 November 2025

findings of Jos et al. (2003) when *Chlorella vulgaris* was exposed to CBZ. Yan et al. (2021) and Qiang et al. (2016) found that exposure to ecologically significant was genotoxic and mutagenic to Chinese rare minnows and zebrafish embryos and larvae. Based on these harmful effects, it is paramount that CBZ is removed from water resources.

Pressure-driven membrane filtration processes (reverse osmosis and nanofiltration) effectively remove CBZ (Cevallos-Mendoza et al., 2022) however the likelihood of membrane fouling, incorrect brine disposal, and high energy demand render these processes unfavourable (Ketharani et al., 2022). The risk of secondary pollution due to the uncontrolled formation of undesirable – and sometimes harmful – by-products is a deterrent to the removal of CBZ through advanced oxidation processes (Chen et al., 2022; Rossi et al., 2023; Puga et al., 2024). Adsorptive removal bypasses the inherent disadvantages of membrane processes and advanced oxidation processes however the simplicity of the process and its effectiveness for removing myriad pollutants. (Mansouri et al., 2021; Yaashikaa et al., 2021)

Adsorption onto natural biomass is a sustainable and potentially cost-effective approach for removing CBZ from water as it involves the use of raw or treated agricultural wastes as biosorbents to remove the contaminants from water. This method promotes a circular economy through waste valorisation. (Elgarahy et al., 2021). Activated carbon and biochar, generated from pyrolysis or carbonisation of biomass, possess high surface area for adsorption which allows for high adsorption capacity (Décima et al., 2021).

Moringa oleifera, known as the "miracle tree", is cultivated in Asia, Africa, and South America. Its roots, leaves, and bark of are used extensively for their medicinal and nutritional value (Pareek et al., 2023). The seed coat has been applied for the removal of various categories of pollutants including heavy metals, dyes, pharmaceuticals and herbicides as presented in Table 1.

Lopes et al. (2022) reported that untreated MO seed coats successfully adsorbed cationic methylene blue dye with a Q_e of 122.7 mg. g^{-1}) despite having a low S_{BET} (3.24 m^2. g^{-1}). This differs significantly from the findings of Adebayo et al. (2019) who were only able to achieve a Q_e of 9.579 mg.g^{-1} of methylene blue with high S_{BET} (1340 m^2.g^{-1}) MO pod husk biochar produced by pyrolysis at 450 °C. The high Q_e reported by Lopes et al. (2022) could be a result of ionic interactions between the cationic dye and negatively charged species on the adsorbent surface. Furthermore, the findings of García-fayos et al. (2016), Jabar et al. (2020) and Gupta et al. (2021) indicate that MO seed coat biosorbent contain -COOH, C—O, *C = O*, N—H, and O—H functional groups which enhance the adsorption of polar contaminants – including heavy metals and herbicides (de Souza et al., 2019). Consequently, most studies report PSO kinetics for the removal of these categories of pollutants (Décima et al., 2021).

Conversely, Quesada et al. (2019) reported a maximum Q_e of 17.48 mg. g^{-1} of neutrally charged acetaminophen (paracetamol) by MO seed coat biosorbent derived by acid treatment with 0.1 M H_3PO_4 followed by carbonisation in a muffle furnace at 300 °C. The high adsorption capacities reported by Farrokhzadeh et al. (2013), Keereerak et al. (2020), and Lopes et al. (2022) for cationic dyes and heavy metals compared to neutrally charged species such as acetaminophen suggests that chemisorption is the driving force for adsorption onto MO seed coat biosorbents.

This present study investigated the performance of MO seed coat-derived biochar as a biosorbent for CBZ in synthetic pharmaceutical wastewater through batch experiments. The synthesised biosorbent was characterised using SEM, EDX, CHNOS, FTIR, BET, and XRD analyses. The effects of operating conditions (agitation speed, adsorption time and adsorption temperature) on the adsorption capacity of the biochar for CBZ were studied. The effects of these variables were first investigated independently through one-factor-at-a-time studies. The effects of parametric interactions on the adsorption of CBZ were investigated through design of experiments conducted using Box-Behnken design with response surface methodology. The OFAT studies informed the ranges of the operating conditions for the design of experiments.

Table 1
Applications of MO seed coat biosorbent.

Category	Adsorbate	Pretreatment	Q_e (mg/g)	Reference
Heavy metal	Cr^{3+}	-	109.6	Farrokhzadeh et al. (2013)
	Cd^{2+}	-	13.1	García-fayos et al. (2016)
Herbicide	Atrazine	0.1 M MeOH, 1.5 % HNO_3, thermal	7.47	Coldebella et al. (2016)
	Diuron	-	3.76	de Souza et al. (2019)
Pharmaceutical	Acetaminophen	0.1 M H_3PO_4, thermal	17.48	Quesada et al. (2019)
	Diclofenac	0.1 M MeOH, 4 % HNO_3, thermal	28.73	Araujo et al. (2018)
Dye	Methylene blue	-	122.7	Lopes et al. (2022)
	Crystal violet	-	156.3	Keereerak et al. (2020)

2. Experimental

2.1. Materials

MO seed pods were obtained from the University of Pretoria plantation. Following particle size reduction, the MO seed coat was subjected to acid pretreatment with 85 % phosphoric acid (H_3PO_4, MM = 97.99 g/mol) from GlassWorld chemicals. CBZ for the batch adsorption experiments was obtained from DLD scientific.

2.2. Apparatus and instruments

Morphological characterization of the biosorbents was performed using Scanning Electron Microscopy (SEM) in a Zeiss Gemini Ultra Plus FEG SEM. Powder samples were thinly dusted on adhesive carbon strips which were placed on SEM carbon stubs. Subsequently, the samples were sputter-coated with carbon to enhance their conductivity. The same Zeiss Gemini Ultra Plus FEG SEM was used for Energy-dispersive X-ray Spectroscopy (EDX/EDS) analysis to determine the surface chemistry of the biosorbents. For the EDX analysis, the biosorbents were dusted on aluminium strips, which were mounted on carbon stubs, and sputter-coated with gold. Carbon-Hydrogen-Nitrogen-Oxygen-Sulphur (CHNOS) analysis was carried out in a Unicube elemental analyser to determine the elemental composition. Fourier-Transform Infrared (FTIR) analysis was performed on a PerkinElmer Spectrum 100 FTIR-ATR spectrometer was set to analyse 32 scans from 4000 cm^{-1} *– 400* cm^{-1}*, with an effective force of 100 on the force gauge.*

The Brunauer-Emmett-Tuller (BET) analysis was carried out on a Micrometrics TriStar II Surface area and porosity analyser. The samples were first degassed in a Micrometrics VacPrep 061 Sample degas system at 77 K *by bubbling with nitrogen to remove any dissolved gases. For the BET analysis, liquid nitrogen was used to maintain an inert environment as well as helium, argon, and nitrogen gas. X-ray diffraction analysis (XRD) was conducted using a PANalytical X'Pert Pro powder diffractometer in θ–θ configuration and Co-Kα radiation (λ=1.789* Å*).*

2.3. Methods

2.3.1. Biosorbent preparation

Raw moringa seed coat was manually separated from the seed kernel, chaff, and seed pod manually. The seed was struck with a pestle to facilitate easier separation of the seed husk from the seed kernel. Peeled kernels and seed husks were stored in separate containers. To

remove sand and dust particles, the seed husks were rinsed 3 times in tap water by stirring with a magnetic stirrer till the supernatant water was almost clear. The husks were then allowed to dry for 48 h at 30 °C in an Ecotherm oven. A mortar and pestle were used to reduce the size of the seed husks before milling in a Retsch PM 100 ball mill for 20 min at 200 rpm. Thereafter, the seed coat was sieved with SABS universal test sieves with mesh sizes of 250 μm, 150 μm, 75 μm in a Fritsch Industriestrasse 8 vibratory sieve shaker. This biomass is hereafter referred to as raw biosorbent.

Particles within the 75–150 μm size range were mixed with 85 % H_3PO_4 at a mass-to-volume ratio of 2.25:1. The resulting paste was left to stand for 24 h to facilitate chemical activation. Subsequently, the activated MO seed coat was transferred into a ceramic crucible was carbonised in a muffle furnace; temperature was increased at 10 °C/min to 600 °C and held at this temperature for 4 h. Carbonised seed coat was cooled to room temperature by natural convection and soaked in deionised water overnight to loosen the complex formed and facilitate removal from the crucible. The retrieved material was rinsed and filtered with a Buchner funnel till the supernatant water had a neutral pH. The sample was dried overnight at 50 °C in an Ecotherm oven. Finally, it was stored in an airtight container to prevent moisture ingress. This sample is hereafter referred to as biochar. The biosorbent subjected to acid activation only (i.e. no subsequent carbonisation) is subsequently referred to as H_3PO_4-mod biosorbent.

2.3.2. Model wastewater preparation and instrument calibration

*CBZ standard solution was prepared by dissolving the required mass of CBZ in deionised water for the desired concentration. For example, for a 50-*ppm *solution, 5* mg *of CBZ was diluted in 1000* mL *of water. To facilitate the dissolution, the mixture was ultrasonicated for 3 h with intermittent shaking. The standard solution was stored in the same container in which it was made. For the batch adsorption experiments, the CBZ concentration was determined using a Hitachi U-3900 UV–Vis spectrophotometer which was operated at* $\lambda = 298$ nm *with a slit width of 2.0* nm. *The CBZ concentration was measured by spectrophotometric method using a calibration curve. Standard solutions of 10* ppm, *20* ppm, *25* ppm, *30* ppm, *40* ppm *were prepared by serial dilution of a 50-*ppm *stock solution. The absorbance of each sample was then correlated to the CBZ concentration.*

The adsorption capacity (Q_t) of CBZ was estimated using the mass balance in Eq(1).

$$\boldsymbol{Q_t} = \frac{(\boldsymbol{C_0} - \boldsymbol{C_t})\boldsymbol{V}}{\boldsymbol{m}} \times 100 \tag{1}$$

where C_0 is the concentration of CBZ at $t = 0$ min (ppm), C_t is the concentration of CBZ after the adsorption time has elapsed, V is the volume of the stock solution used for the experiment (L) and m is the mass of the adsorbent used (g). The equilibrium adsorption time was the time after which no further adsorption took place despite higher agitation speed or temperature. The concentration of CBZ at this time was C_e (ppm). The percentage removal is calculated as

$$\%R = \frac{\boldsymbol{C_0} - \boldsymbol{C_t}}{\boldsymbol{C_0}} \times 100 \tag{2}$$

2.3.3. Batch adsorption experiments

Batch adsorption experiments were conducted to evaluate the performance of the synthesised biosorbent. 50 mL of the 50-ppm stock solution was placed in a 50 mL conical flask, followed by the addition of 50 mg of biosorbent. The mixture was immediately agitated at 200 rpm for the required duration (hours) at a controlled temperature in an incubator shaker. The agitation speed was adjusted using the control buttons on the shaker. After the adsorption time had elapsed, the water samples were filtered through filter paper to remove solid particles which would scatter light and distort the UV–Vis absorbance readings. The spent biosorbent was then recovered and dried overnight at 50 °C.

2.4. Adsorption performance of MO biochar

2.4.1. Effect of variables using OVAT

50 mL of 50-ppm stock solution was placed in a conical flask and 50 mg of biochar was added. The conical flask was sealed with aluminium foil and shaken an incubator shaker at a constant speed for the required duration.

The effect of agitation speed was studied at 100 rpm, 200 rpm, 300 rpm and 400 rpm. 50 mg of biochar was added to 50 mL of a 50-ppm CBZ solution and agitated at the selected speed for 3 h at a controlled temperature of 30 °C. The effect of temperature was studied at 30 °C, 40 °C and 50 °C; the agitation speed and time were 200 rpm and 3 h, respectively. The effect of adsorption time was studied through a series of experiments at adsorption times of 15 min, 30 min, 1 hour, 2 h and 3 h; the agitation speed and temperature were held at 200 rpm and 30 °C, respectively.

Once the required time had elapsed, the conical flask was removed from the incubator. The spent biosorbent was then separated out of the model wastewater sample by filtration using filter paper. The spent biosorbent was subsequently dried in an oven at 50 °C for 24 h. 3 mL of the supernatant sample was collected for UV–Vis spectrophotometry to determine the CBZ concentration.

2.4.2. Effect of operating variables using statistically designed experiments

The Box-Behnken experimental design factors are presented in Table 2. This design was selected as it could accurately predict model parameters with fewer experimental runs.

2.4.3. Model development

Quadratic regression models Eq (3) are often used to quantify the effect of parametric interactions on response variables.

$$Y_i = \beta_0 + \beta_A A + \beta_B B + \beta_C C + \beta_{AB} AB + \beta_{AC} AC + \beta_{BC} BC + \beta_{AA} A^2 + \beta_{BB} B^2 + \beta_{CC} C^2 \tag{3}$$

where Y_i is the predicted value of the response, β_0 is the global average of the response, β_i is the regression coefficient of the main factors and β_{ii} is the regression coefficient of the interaction of the factors (Regti et al., 2017). The goodness-of-fit of the quadratic model is evaluated using the correlation coefficient (R^2), adjusted R^2, p-value, F-value, SSE, MSE, the residual, and the corrected total.

A coefficient of determination (R^2) close to 1 is desirable; R^2 can increase or remain the same with the introduction of a new independent variable (Starbuck, 2023). Conversely, the adjusted R^2 will either decrease or remain the same when a new independent variable is introduced. The coefficient of variation (CV %) is a ratio of the standard error to the mean value of the response (Regti et al., 2017); CV % < 10 % indicates reliability of the experiments conducted. A good model fit should have an adequate precision (AP) >4 (Agarwal et al., 2016). The sum of squared error (SSE) is the square of the difference between the experimental data, and the model predicted data. A lower SSE is desirable as it indicates that the model prediction is close to the experimental data. The mean square error (MSE) is the average of the squared errors for each data point. A Lower MSE is desirable. In conjunction with the SSE and MSE, the p-value and F-value are used to evaluate the extent of contribution of the model variables and their interactions.(Starbuck, 2023)

Table 2
Experimental factors and levels for Box-Behnken experimental design.

	−1	0	1
Agitation speed (rpm)	200	300	400
Adsorption time (hours)	1	2	3
Adsorption temperature (°C)	30	40	50

The F-value is the ratio of the model mean square error to the error mean square. A high F-value ($F > 1$) indicates a statistically significant model (Ali et al., 2018; Starbuck, 2023). The significance of the operating parameters on the dependent variables using the p-value which was determined with a 95 % confidence interval. For a parameter to have a significant effect, $p < 0.05$ is essential.

2.4.4. Model validation

Welch's *t*-test was used to evaluate the reliability of the quadratic regression model by comparing the means of $q_{e,\ experimental}$ and $q_{e,\ predicted}$. Firstly, the null hypothesis which suggests that both data sets have the same mean was assumed i.e.

$$\mu_1 = \mu_2 \tag{4}$$

where μ_1 and μ_2 are the mean values of the two data sets being considered. The variances were estimated with

$$\sigma^2 = \frac{\sum_{i=1}^{n} (x_i - \mu)^2}{n} \tag{5}$$

where n is the number of data points in the set, x_i is the specific data point (Starbuck, 2023). The standardised difference (T) between the means was determined using

$$T = \frac{\overline{X_1} - \overline{X_2}}{\sqrt{\frac{{\sigma_1}^2}{n_1} - \frac{{\sigma_2}^2}{n_2}}} \tag{6}$$

where $\overline{X_1}$ is the average value of the first sample set ($q_{e,\ experimental}$) and $\overline{X_2}$ is the average value of the second sample set ($q_{e,\ predicted}$). ${\sigma_1}^2$ and ${\sigma_2}^2$ are the variance of the data sets, respectively. n_1 and n_2 are the number of data points in each data set, respectively. An adjusted degrees of freedom (ν) must be estimated since the variance (σ^2) of the data sets were not equal.

$$\nu = \frac{\left(\frac{{\sigma_1}^2}{n_1} + \frac{{\sigma_2}^2}{n_2}\right)}{\frac{\left(\frac{{\sigma_1}^2}{n_1}\right)}{n_1 - 1} + \frac{\left(\frac{{\sigma_2}^2}{n_2}\right)}{n_2 - 1}} \tag{7}$$

Finally, the probability (P ($T \leq t$)) was determined as the area under the t-distribution curve at a particular test statistic, t. The p-value was determined using the two-tailed test such that

$$p = 2 \times \min(P(T \leq t_{obs}),\ 1 - (P(T \leq t_{obs})) \tag{8}$$

The null hypothesis was rejected if $p \leq 0.05$ thus indicating that the difference between the means of the data sets was statistically significant. Conversely, if $p > 0.05$ it was concluded that the difference between the means was not statistically significant, and the null hypothesis could not be rejected (Starbuck, 2023). For this study, the *t*-test was conducted using the Data analysis add-in Microsoft Excel.

2.4.5. Optimisation

The Derringer–Suich desirability function approach and gradient-based numerical search algorithms were applied for the optimisation. Each response was firstly converted to a desirability value, d, between 0 and 1. The goal of the optimisation was to maximise the response by adjusting the global desirability function (D) which was developed based on individual desirability functions (d_i) given by Eq (9).

$$d_i = \begin{cases} 0, & y_1 < L \\ \left(\frac{y_1 - L}{T - L}\right)^r, & T \leq y_1 \leq L \\ 1, & y_1 > T \end{cases} \tag{9}$$

where d_i is the dimensionless desirability, y_1 is the predicted response value, T is the target value, L is the upper limit of predicted results, and r is the shape factor and is equal to 1 (Gamero-Salinas et al., 2025). The global desirability function was estimated using the geometric mean of individual desirability functions as shown in Eq (10).

$$D = \left(\prod_{i=1}^{k} d_i y_i\right)^{1/k} \tag{10}$$

where k is the number of individual desirability functions. The gradient-search algorithm approach maximises the global desirability function by recurrently adjusting the independent variable levels within the design space (Marinković, 2021). Design Expert 13 software was used for the adsorption optimization in this study.

2.5. Kinetic and isotherm studies

2.5.1. Adsorption isotherms

The Langmuir isotherm model describes monolayered heterogeneous adsorption where all adsorbent particles have equal enthalpy of adsorption. Eq (11) in the standard Langmuir isotherm equation.

$$q_e = \frac{q_m K_L C_e}{1 + K_L C_e} \tag{11}$$

Here, q_e is the equilibrium adsorption capacity (mg/g), C_e is the equilibrium concentration of adsorbate in solution (g/L), q_m is the maximum adsorbate concentration in the adsorbent when surface sites are saturated (g/g), and b_m is the Langmuir adsorption constant of the adsorbate species (Décima et al., 2021). Along with the Langmuir model, the Freundlich model is the most used isotherm model for describing adsorption with biosorbents. It describes multilayer, heterogeneous adsorption and is represented by Eq (12).

$$q_e = K_F C_e^{\frac{1}{n}} \tag{12}$$

K_F is the Freundlich adsorption capacity parameter in $(mg/g)(L/g)^{1/n}$ and n is a unitless coefficient (Décima et al., 2021). The Sips isotherm in Eq (13) also combines the Langmuir and Freundlich isotherm models and describes heterogeneous adsorption thus limiting the increase of the adsorption capacity.

$$q_e = \frac{q_{ms} K_S {C_e}^{n_S}}{1 + K_S {C_e}^{n_S}} \tag{13}$$

where n_s is the index of heterogeneity, a value between 0 and 1. K_s is the Sips constant (L/mg) and q_{ms} is the maximum adsorption capacity in mg/g. The Dubinin-Radushkevich (D-R) similarly assumes heterogeneous adsorption. This model is described by Eq (14).

$$q_e = q_m e^{-\beta\varepsilon} \tag{14}$$

where q_m is the maximum adsorption capacity in mg/g, β is the average free energy for adsorption per mole of adsorbate (kJ/mol) and ε is the Polanyi potential given by Eq (15).

$$\varepsilon = RT\ln\left(1 + \frac{1}{C_e}\right. \tag{15}$$

where R is the ideal gas constant (8.314 J/(kmol.K)), T is the adsorption temperature (K), and C_e is the equilibrium adsorbate concentration (mg/L). The D-R model explicitly correlates the adsorption capacity to the square of temperature and is typically used to estimate the free energy of adsorption. This in turn can be used to distinguish between chemisorption and physisorption as the driving force for adsorption. (Ayawei et al., 2017)

Bhattacharya et al. (2020) found that CBZ adsorption onto graphene oxide nanoplatelets best fit the Temkin isotherm model presented in Eq (16). This isotherm assumes a heterogeneous adsorbent surface with uniform distribution of energy across each binding site in an adsorbent

and is described by

$$q_e = B ln(k_T \quad (16)$$

where k_T is the Temkin isotherm constant and B is the dimensionless Temkin constant estimated using Eq (17).

$$B = \frac{RT}{b} \quad (17)$$

with b being the enthalpy of adsorption in J/mol and T being the adsorption temperature (K) (Serafin et al., 2023).

2.5.2. Adsorption kinetics

The pseudo-first order (PFO) model in Eq (18) describes an irreversible reaction where adsorption rate is directly proportional to the number of unoccupied sites (Décima et al., 2021) and adsorption enthalpy is independent of adsorbent surface coverage and adsorbed ions do not interact (Largitte et al., 2016).

$$q_t = q_e\left(1 - e^{-k_1 t}\right) \quad (18)$$

Here, q_t is the amount of adsorbate that is adsorbed at time t (mg/g), q_e is the amount of adsorbate that is adsorbed at equilibrium (mg/g) and k_1 is the adsorption rate constant (L/min).

The pseudo-second order (PSO) model in Eq (19) describes an adsorption process driven by chemisorption. The adsorption rate depends on the adsorption capacity and is proportional to the square of the number of unoccupied sites.

$$q_t = \frac{k_2 {q_e}^2}{1 + k_2 q_e t} \quad (19)$$

where k_1 is the adsorption rate constant (g/(mg.min)). The Elovich kinetic model (Eq (20)) proposes that adsorption is multilayered and that the adsorption rate decreases exponentially as the number of unoccupied sites decreases. (Ayawei et al., 2017)

$$q_t = \alpha \ln(a\alpha) + \alpha ln t \quad (20)$$

where a (mg/(g.min)) and α (mg/g) are the Elovich constants.

The intraparticle diffusion model assumes that the migration of adsorbate particles from the boundary layer to the pores of an adsorbent is the driving force for adsorption. For this model, the adsorption capacity at time t is calculated as

$$q_t = k_{IP}\, t^{1/2} \quad (21)$$

where k_{IP} is the intraparticle diffusion rate constant in mg/g.min$^{-0.5}$ and t is the adsorption time (min). If the plot of q_t vs $t^{1/2}$ is linear, it indicates that intraparticle diffusion is the rate-determining step for adsorption.

2.5.3. Model fitting

To determine which isotherm model provided a better fit, the R^2 was calculated using Eq (22).

$$R^2 = 1 - \frac{E_1}{E_2} \quad (22)$$

where E_1 and E_2 are estimated using Eq (23) and Eq (24).

$$E_1 = \left(q_{e,\ fit} - q_{e,\ data}\right)^2 \quad (23)$$

$$E_2 = \left(q_{e,\ fit,\ avg} - q_{e,\ data}\right)^2 \quad (24)$$

The model parameters were estimated by calculating E_1 and E_2 for each data point and then minimising these errors by changing the guessed parameters using the Solver feature in Microsoft Excel. The model which provided the best fit would be the one with the highest R^2. The more suitable kinetic model was determined by comparing the R^2 values of model fits obtained using trendlines on Microsoft excel graphs.

3. Results and discussion

3.1. Characterisation

3.1.1. Morphology (SEM)

The amorphous morphology of MO seed coat changed significantly following acid hydrolysis and carbonisation as shown in Fig. 1. The resultant biochar consisted of aggregated carbon nanospheres as well as some irregularly shaped structures. Lee et al. (2019) reported similar morphological structures of their carbon black, which is typically produced through pyrolysis at temperatures of 1100 °C – 1300 °C (Jiang et al., 2024).

3.1.2. Surface chemistry and elemental composition (EDX and CHNOS)

Acid hydrolysis and carbonisation decreased the H/C ratio producing biochar with greater aromaticity (Domingues et al., 2017b; Wijitkosum et al., 2019; Décima et al., 2021). The reduction of the O/C and $(O + N)$/C ratio indicate increased hydrophobicity due to loss of polar functional groups in the biochar compared to the raw biosorbent (Tan et al., 2015).

The biochar synthesised has the highest carbon content and the lowest oxygen and hydrogen content of the three biosorbents in Table 3. Consequently, it has the lowest H/C, O/C, and $(O + N)$/C ratio of the three biosorbents. It is therefore the most non-polar, hydrophobic, and aromatic of the three biosorbents and thus best suited for CBZ removal. (Fig. 2)

3.1.3. Surface functionality (FTIR)

Fig. 3 depicts the FTIR spectra of the biosorbents synthesised in this study. The weak, broad peak at 3321 cm^{-1} in the raw biosorbent and

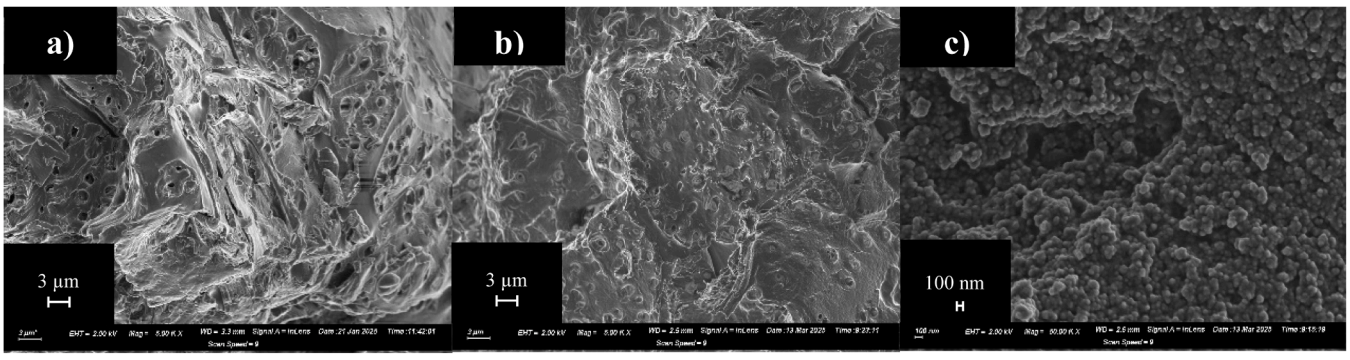

Fig. 1. SEM micrographs of synthesised biosorbents.

Table 3
Elemental analysis of the biosorbents synthesised.

Biosorbent	% C	% H	% N	% O	% S	H/C	O/C	(O + N)/C
Raw	52.3	7.10	2.50	44.7	0.50	0.14	0.85	0.902
H_3PO_4-mod	54.7	6.90	0.80	37.4	0.20	0.13	0.68	0.698
Biochar	59.6	2.10	1.50	36.7	0.10	0.04	0.62	0.641

3340 cm^{-1}, in the H_3PO_4-mod biosorbent, is attributed to O—H bond stretching. The strong, narrow peaks at 2929 cm^{-1} and 2851 cm^{-1}, in the raw biosorbent, and 2924 cm^{-1} and 2848 cm^{-1}, in the H_3PO_4-mod biosorbent, are attributed to C—H stretching vibrations. The peaks at 1661 cm^{-1} and 1655 cm^{-1}, in the raw and H_3PO_4-mod biosorbents, respectively, corresponds to $C = C$ stretching in a cyclic alkene, this aids π- π interactions with aromatic rings in CBZ. The peaks observed at 1034 cm^{-1} and 1030 cm^{-1} and between 1200 cm^{-1} and 1300 cm^{-1} in the raw and H_3PO_4-mod biosorbents correspond to C—O stretching in an aromatic ester (LibreTexts Chemistry, 2024) – which could also aid in CBZ adsorption via π- π interactions. The rice husk biosorbent generated by Aghababaei et al. (2021) exhibited a peak at 1230 cm^{-1} which corresponds to C—O-C ether bond stretching vibrations in esters or aldehydes This confirms the formation of aldehydes and ketones during acid treatment of biomass and ester bonds facilitate the cross-linking of lignin and hemicellulose within biomass as suggested by Jönsson et al. (2016).

The FTIR spectrum of the biochar lacks the O—H stretching and C—H stretching vibrations between 2800 cm^{-1} and 3600 cm^{-1} in the raw and H_3PO_4-mod biosorbents. The peak at 1573 cm^{-1} represents $C = C$ stretching in a cyclic alkene (LibreTexts Chemistry, 2024) and the shift from 1655 cm^{-1} in the H_3PO_4-mod biosorbent is due to higher degree of condensation of the aromatic structures in the biosorbent Zeghioud et al., 2022). The peak at 1132 cm^{-1} and 989 cm^{-1} corresponds C—O stretching vibrations and $C = C$ bending in an alkene, respectively (LibreTexts Chemistry, 2024).

3.1.4. Crystallinity (XRD)

The X-ray diffractogram of the biochar exhibited broad peaks at 2Θ = 28° and 51° The peak at 28° is a reflection of the (002) plane of graphitic or turbostratic carbon, while the peak at 51° is the reflection of the (004) plane representing graphitic carbon (Chen, 2020). The peak shifts when compared to biochar in literature are typically attributed to silica or carbonate impurities (Domingues et al., 2017a; Kritikaki et al., 2025). However EDX (Fig. 2) and XRD (Fig. 4) analyses detected minimal impurities; thus confirming Chen (2020)'s explanation.

3.1.5. Textural properties (BET)

The hysteresis curves of the raw biosorbent and the biochar are presented in Fig. 5a and Fig. 5b, respectively. The raw biosorbent exhibits a type II N2 adsorption/desorption isotherm which is characteristic of a non-porous absorbent while the biochar exhibits a type IV isotherm characteristic of mesoporous adsorbents. However, the biochar exhibits a type H4 hysteresis loop which indicates the presence of narrow, slit-like pores in a microporous biosorbent. The type IV isotherm and H4 hysteresis loop indicate that the biochar has significant micropore (< 2 nm) and mesopore (2 – 50 nm) fractions which would aid in adsorption of CBZ (Sing et al., 1985).

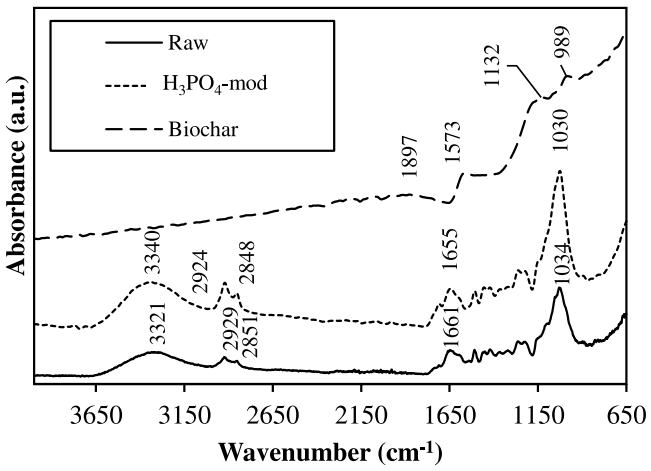

Fig. 3. FTIR spectra of biosorbents.

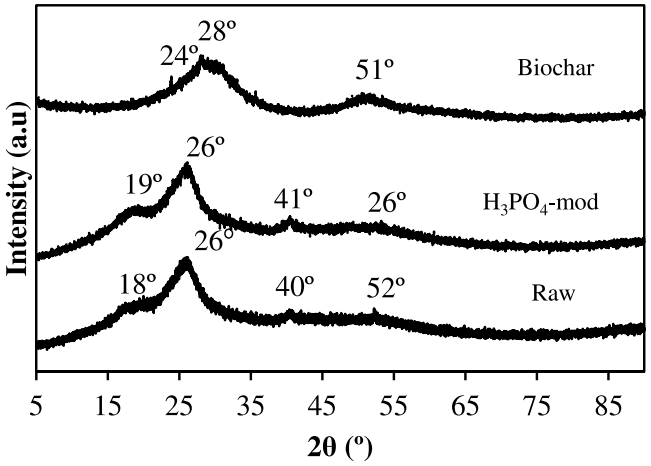

Fig. 4. X-ray diffractograms of biosorbents.

The specific surface area (S_{BET}), total pore volume (V_T) and average pore diameter (D_{Avg}) are presented in Table 4. Acid hydrolysis and carbonization increased S_{BET} of the raw biosorbent from 1.16 m^2/g to 237.3 m^2/g. Wang et al. (2020) reportedly produced biochar with S_{BET} = 659.6 m^2/g through H_3PO_4 hydrolysis and subsequent pyrolysis at 600 °C.

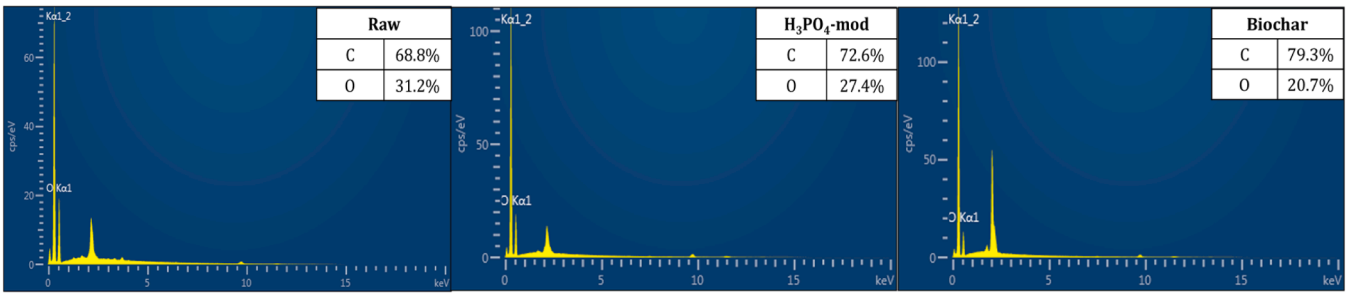

Fig. 2. EDX analysis of synthesised biosorbents.

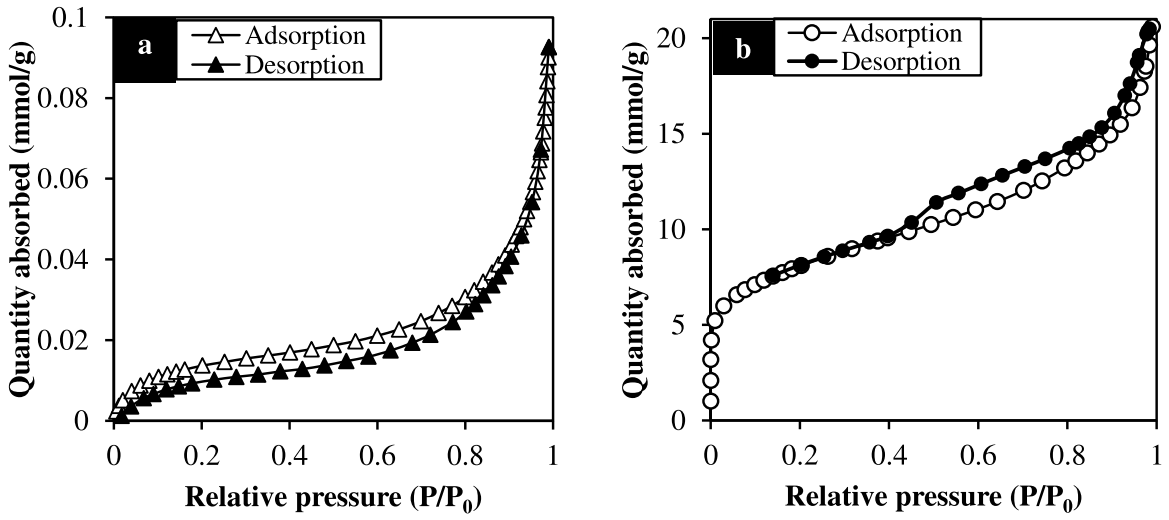

Fig. 5. N2 adsorption and desorption isotherms of a) raw biosorbent and b) biochar.

Table 4
Textural properties of the raw biosorbent and biochar from BET analysis.

Biosorbent	S_{BET} (m^2/g)	V_T (cm^3/g)	D_{Avg} (Å)
Raw	1.160	0.0028	97.52
Biochar	237.3	0.1814	30.57

3.2. Effect of variables using OVAT

3.2.1. Effect of adsorption time

The effect of adsorption time was studied at an agitation speed of 200 rpm, 30 °C as presented in Fig. 6. A fast adsorption rate is observed up to 60 min due to the rapid occupation of abundant adsorption sites (Naghdi et al., 2019; Lopes et al., 2022). Afterwards the adsorption rate slows down up to 120 min as surface adsorption sites are filled up. In this phase, intraparticle diffusion (i.e. pore diffusion) drives the adsorption process (Aghababaei et al., 2023). After 120 min, 93.3 % of CBZ had been removed and equilibrium was reached; minimal adsorption took place after this time. This supports the findings of Naghdi et al. (2019) who reported that their pinewood nanobiochar removed 95 % of CBZ in under 3 h of adsorption.

3.2.2. Effect of agitation speed

Faster agitation speed results in a thinner external boundary layer, increased mass transfer across the boundary layer and a higher adsorption rate (Naghdi et al., 2019). The effect of agitation speed on the adsorption capacity was evaluated at a constant temperature (30 °C) and adsorption time (3 hrs). Fig. 7 presents the findings of the adsorption experiments.

Increasing the agitation speed from 100 to 200 rpm increased the adsorption capacity by 6.94 %. A lower increase (4.76 %) occurred between 200 rpm and 300 rpm and the highest increase (8.61 %) occurred between 300 and 400 rpm. The maximum adsorption capacity was obtained at an agitation speed of 400 rpm. These suggest that agitation speed influences the adsorption capacity as reported in literature (Naghdi et al., 2019; Aghababaei et al., 2023; Agilandeswari et al., 2024).

3.2.3. Effect of adsorption temperature

The effect of adsorption temperature was evaluated at a constant agitation speed of 200 rpm and adsorption time of 3 h. The results of the OVAT experiments conducted are presented in Fig. 8. The adsorption capacity increased from 44.58 mg/g to 45.23 mg/g when the temperature increased from 30 °C to 40 °C. A more significant 6.88 % increase from 45.23 mg/g to 48.34 mg/g occurred with increase from 40 °C to 50 °C. The highest adsorption capacity was obtained at 50 °C. Similarly, Agilandeswari et al. (2024) reported an increase in the percentage removal of CBZ when the temperature was increased from 30 °C to 50 °C and Aghababaei et al. (2023) also reported an increase in CBZ adsorption onto flax shives and oat hull-derived hydrochar with an increase in temperature from 20 °C to 40 °C. The increase in CBZ removal was attributed to reduction of the viscosity of water at higher temperature and increased the rate of CBZ diffusion through the external boundary

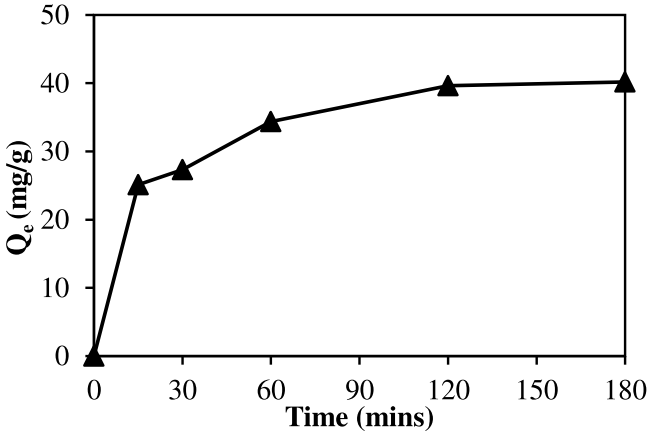

Fig. 6. Effect of adsorption time on adsorption capacity for CBZ.

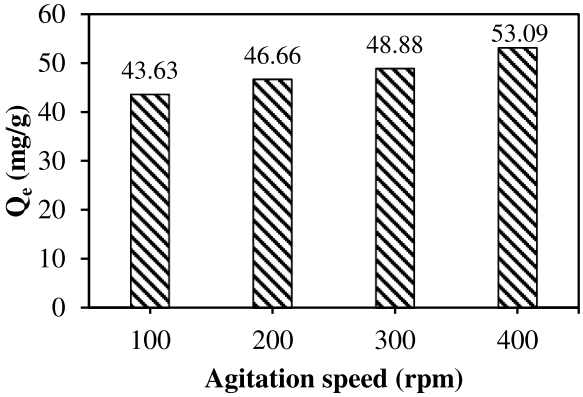

Fig. 7. Effect of agitation speed on adsorption capacity.

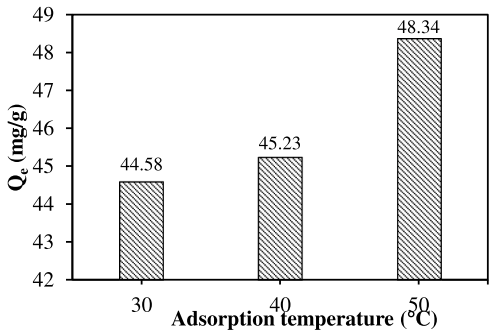

Fig. 8. Effect of temperature on adsorption capacity.

Table 5
Fit statistics for quadratic regression models.

Parameter	Value
R^2	0.9754
R^2 -adjusted	0.9015
CV %	2.27
AP	11.90

Table 6
ANOVA of quadratic regression model for adsorption capacity.

Source	d_f	SSE	MSE	F-value	p-value
Model	9	132.8	14.76	13.20	0.028
A-Agitation speed	1	57.56	57.56	51.48	0.006
B-Temperature	1	2.128	2.128	1.903	0.262
C-Time	1	2.993	2.993	2.677	0.200
AB	1	4.584	4.584	4.100	0.136
AC	1	1.768	1.768	1.581	0.298
BC	1	2.863	2.863	2.560	0.208
A^2	1	0.977	0.977	0.874	0.419
B^2	1	30.83	30.83	27.57	0.013
C^2	1	4.417	4.417	3.950	0.141
Residual	3	3.354	1.118		
Cor Total	12	136.2			

layer of the adsorbent – suggesting endothermic adsorption of CBZ.

3.3. Effect of operating variables using statistically designed experiments

3.3.1. Model development

Eq(25) is the quadratic regression model fit for the adsorption capacity.

$$Qe = 79.47 + 0.09557\,A - 2.734\,B + 0.7936\,C - - 0.001071\,AB + 000.6648\,AC + 0.08406\,BCE$$

$$- - 0.00006537\,A2 + 0.03673\,B2 - 1.390\,C2 \quad (25)$$

Based on the high coefficient of determination (R^2) and adjusted R^2 is <10 % the model describes the experimental data well. The precision of the model is confirmed by coefficient of variance (CV %) <10 % and adequate precision (AP) > 11, as seen in Table 5. (Table 6, 7)

3.3.2. ANOVA of quadratic regression model

The ANOVA (Table 6) confirms the OVAT result that agitation speed influences adsorption capacity significantly based on the p-value of 0.006 in Table 6. This supports the findings of Aghababaei et al. (2023) and Agilandeswari et al. (2024) that agitation speed directly influences CBZ removal. According to the ANOVA, temperature and adsorption time do not significantly affect CBZ adsorption contrary to the OVAT results. However, the square of the temperature was found to be statistically significant with $p = 0.015 < 0.05$. This phenomenon indicates that temperature affects adsorption capacity quadratically rather than in a linear manner as explained by the Dubinin-Radushkevich isotherm model in Eq(14).

Table 7
t-Test for $q_{e,\ experimental}$ and $q_{e,\ predicted}$.

	$q_{e,\ experimental}$ (mg/g)	$q_{e,\ predicted}$ (mg/g)
Mean (μ)	46.58	46.51
Variance (σ^2)	11.35	11.02
Observations	13	13
Hypothesised Mean Difference	0	
V	24	
T	0.05138	
P($T \leq t$) two-tail	0.9594	

Table 8
Comparison of mf400odel prediction to experimental data at optimum adsorption conditions.

	Value
$Q_{e,\ predicted}$ (mg/g)	51.87
$Q_{e,\ experimental}$ (mg/g)	51.09
% Error	1.53

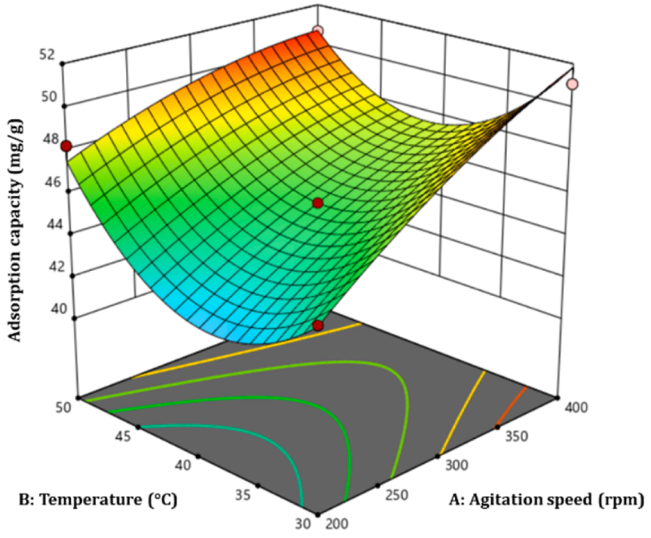

Fig. 9. Response of adsorption capacity to temperature and agitation speed at time = 2 h.

The effects of the interactions between the operational conditions on the adsorption capacity is represented in 3D surface plots (Figs. 9-11). After an agitation time of 2 h the adsorption capacity increases with a change in the agitation speed – regardless of the temperature. The highest removal is obtained at a high agitation speed (400 rpm) and a low temperature (30 °C).

The effect of the interaction of agitation speed and adsorption time is best observed at a constant temperature of 30 °C. The highest adsorption capacity was obtained after a short period of time (1 hour) at a high agitation speed (350 rpm) (Fig. 9). At a constant agitation speed of 300 rpm, adsorption capacity does not vary appreciably when adsorption time is varied (Fig. 10); the adsorption temperature has a greater influence on the adsorption capacity at a constant agitation speed. This is not expected considering the p-value of temperature (0.262) is higher than that of time (0.200) from the model fit which should indicate that temperature has a less significant effect than adsorption time (Fig. 11).

3.3.3. Model validation

A *t*-test was conducted to validate the model, and the results of the *t*-test are presented in Table 7. For this study, $P(T \leq t) = 0.9594 > 0.05$ (Starbuck, 2023) indicating that the difference between the model prediction and the experimental data is not statistically significant. The

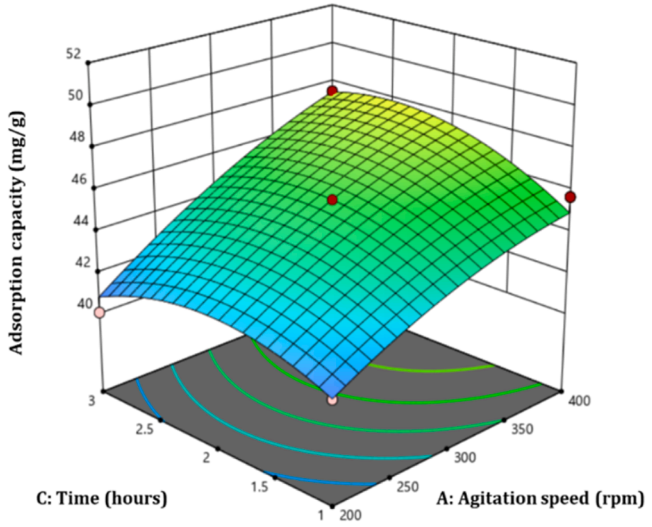

Fig. 10. Response of adsorption capacity to changing time and agitation speed at temperature = 40 °C.

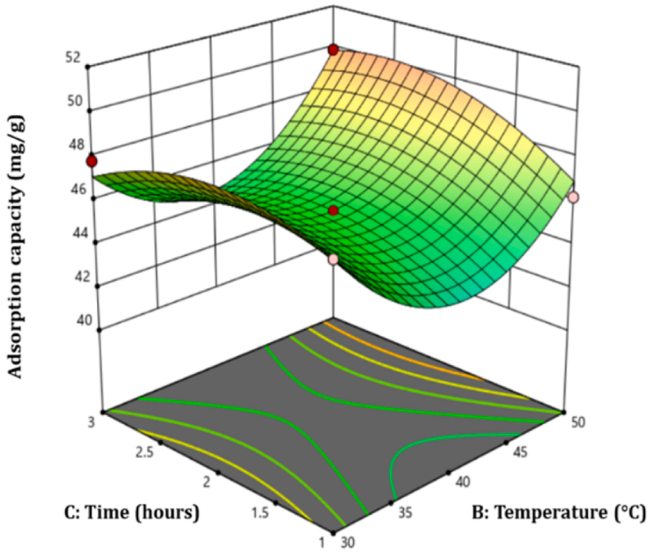

Fig. 11. Response of adsorption capacity to changing time and temperature at an agitation speed of 300 rpm.

quadratic regression model adequately predicted the adsorption capacity within the BBD design space (refer to Table 2).

3.3.4. Optimisation

The optimisation conducted predicted a maximum adsorption capacity of 51.87 mg/g at 400 rpm, 30 °C after 2.15 h. This prediction was validated by comparing it to experimental results at the predicted optimum conditions as presented in Table 8. The experimental result is within 5 % of the model prediction thus confirming the reliability of the prediction. Next, the changes in the biochar surface functionality due to adsorption at the optimum conditions were studied through FTIR.

The purity of the CBZ used for this work was confirmed by peaks at 3465 cm^{-1}, 1675 cm^{-1}, and 1376 cm^{-1} in Fig. 13. This spectrum was compared to the post-adsorption biochar spectrum in Fig. 12. The intensity of the biochar FTIR peaks reduced significantly after CBZ adsorption – suggesting lower concentration of these functional groups on the biosorbent surface due to adsorption (Pasieczna-Patkowska et al., 2025). Additionally, notable peak shifts occurred from 939 cm^{-1} to 975 cm^{-1} and 3068 cm^{-1} to 3104 cm^{-1}. The peak at 939 cm^{-1} corresponds to *C* = *C* bending (LibreTexts Chemistry, 2024) and the peak at 3068 cm^{-1} is

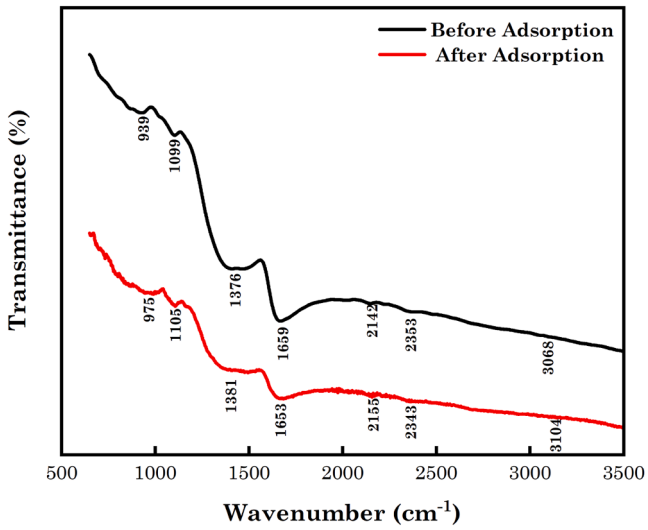

Fig. 12. Post-adsorption FTIR of MO biochar.

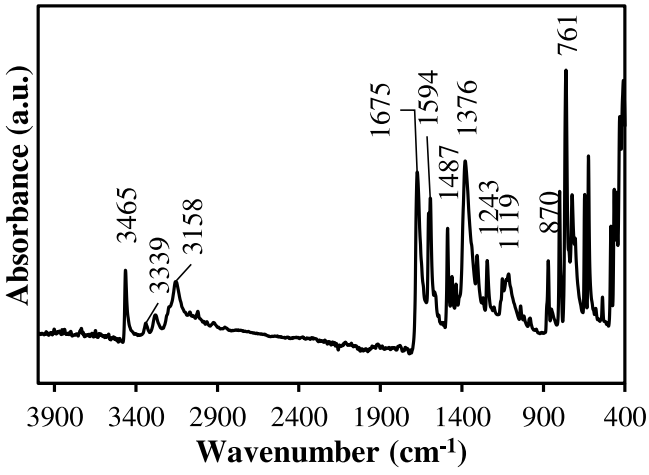

Fig. 13. FTIR spectrum of CBZ.

attributed to O—H bending (Quesada et al., 2019). The shift of these peaks to higher wavenumbers could indicate binding of these functional groups to other species including pollutants (Ellerbrock et al., 2021). The post-adsorption FTIR confirms CBZ adsorption onto the adsorption surface, particularly via chemisorption.

3.4. Adsorption kinetics and isotherms

The adsorption kinetic and isotherm studies were conducted at 400 rpm, 50 °C up to 2 h of adsorption. The results of adsorption isotherm model fits presented in Fig. 14 and Table 9 indicate that the adsorption is best described by the Temkin isotherm model, suggesting reversible adsorption with a linear decrease in the heat of adsorption as more adsorption sites are occupied (Baghdadi et al., 2016; To et al., 2019). The adsorption kinetic model fits presented in Fig. 15 and

Table 10, the PSO describes the experimental data best; indicating chemisorption as the driving force for the adsorption with the adsorption rate being proportional to the number of unoccupied adsorption sites. This finding corroborates the findings of the studies by Shin et al. (2020) who studied CBZ adsorption onto biochar generated from coffee grounds and Nezhadali et al. (2022) who investigated CBZ adsorption onto a polypryole-chitosan composite adsorbent.

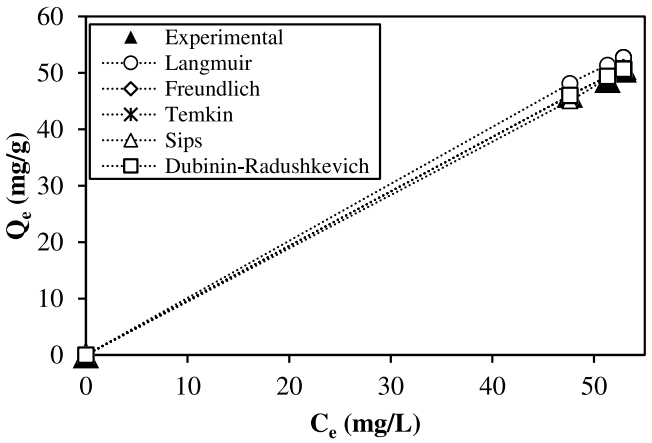

Fig. 14. Adsorption isotherm fits vs experimental data.

Table 9
Adsorption isotherm model fits.

Model	
Langmuir	
K_L (L/g)	0.002963
q_m (mg/g)	389.0
R^2	0.9998
SSE	0.3368
Freundlich	
K_F (mg/g)(L/g)$^{1/n}$	1.292
n_F (mg/g)	1.081
R^2	0.9998
SSE	0.4161
Temkin	
b (kJ/mol)	60.49
K_T (L/g)	0.05917
R^2	0.9999
SSE	0.3007
Sips	
q_m (mg/g)	2.068
K_S	0.3185
n_S	1.176
R^2	0.9994
SSE	1.560
Dubinin-Radushkevich	
β (kJ/mol)	0.0001655
Q_m (mg/g)	77.02
R^2	0.9998
SSE	0.5233

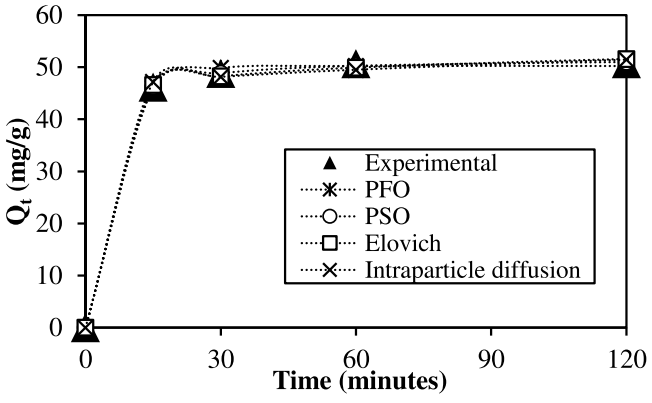

Fig. 15. Adsorption kinetic model fit for experimental adsorption data at 400 rpm and 50 °C.

Table 10
Adsorption kinetic model fits for the experimental data.

Model	
Pseudo-first order	
k_1 (min^{-1})	−0.1648
q_e (mg/g)	50.23
R^2	0.9992
SSE	1.573
Pseudo-second order	
k_2 (g.(mg.min^{-1}))	0.01073
q_e (mg/g)	51.77
R^2	0.9999
SSE	0.2840
Elovich	
a (mg.(g.min^{-1}))	7.52 × 10^6
α (mg/g)	2.40
R^2	0.9947
SSE	1.877
Intraparticle diffusion	
k (mg/(g.min$^{0.5}$))	0.6021
C (mg/g)	44.86
R^2	0.9983
SSE	3.404

3.5. Comparison with other adsorbents

The biochar synthesised in this study achieved a maximum adsorption capacity of 51.09 mg CBZ/g biosorbent and is compared to other adsorbents in Table 11. This value is comparable to the adsorption capacity of organoclays (34.34 mg/g) reported by Viegas et al. (2024) and the adsorption capacity of rice husk biochar (40.0 mg/g) reported by Liu et al. (2013). These adsorption capacities are however dwarfed by the adsorption capacity of biochars obtained from pomelo peels (286.5 mg/g) and leather shavings (133.0 mg/g) as reported by Chen et al. (2017a) and Marques et al. (2022). The highest adsorption capacity (684.8 mg/g) was obtained using giant macroporous silica (Alver et al., 2024) while rice husk biochar had the lowest maximum adsorption capacity (14.81 mg/g). The biochar produced for this study is therefore a promising adsorbent for CBZ removal.

4. Conclusion

Acid hydrolysis of MO seed coat with H_3PO_4 for 24 h and subsequent

Table 11
Adsorption capacity of various biosorbents.

Adsorbent	Q_m (mg/g)	u (rpm)	T (°C)	t (hours)	Reference
Macroporous silica	684.8	150	22	1.5	(Alver et al., 2024)
Peanut shell biochar	14.81	120	Ambient	168	(Chen et al., 2017b)
Pomelo peel biochar	286.5	180	25	24	(Chen et al., 2017a)
Rice husk biochar	40.0	180	28	2	(Liu et al., 2013)
Peach stone activated carbon	242	250	39	4	(Álvarez-Torrellas et al., 2017)
Leather shavings biochar	133	150	25	24	(Marques et al., 2022)
Modified hydrochar	376.1	-	-	-	(Zhong et al., 2025)
Organoclay	34.34	110	25	24	(Viegas et al., 2024)
Polypyrole-chitosan nanocomposite	122.0	400	25	0.417	(Nezhadali et al., 2022)
MO seed coat biochar	51.09	400	30	2	This study

carbonisation at 600 °C for 4 h produced biochar with good physico-chemical properties for adsorption. The surface area, surface functionality, crystallinity, and elemental composition of the biochar enhance its CBZ adsorption potential. The effect of operating parameters on the adsorption capacity were studied OVAT and through Box-Behnken experimental design with response surface methodology. Statistical ANOVA confirmed the reliability of a quadratic regression model for the prediction of the adsorption capacity of CBZ onto MO seed coat biochar. Agitation speed significantly influences adsorption capacity unlike temperature and adsorption time. The optimum adsorption conditions were found to be 400 rpm, 30 °C, and 2.15 h. adsorption was best described by pseudo-second order kinetics and the Temkin isotherm model. MO seed coat-derived biochar is an effective biosorbent for CBZ adsorption from model wastewater. Future work should investigate the biochar performance in real wastewater systems and further inform on the mechanism of adsorption of CBZ and other pharmaceuticals onto biochar.

CRediT authorship contribution statement

Peace S. Azeh: Writing – original draft, Visualization, Methodology, Investigation, Formal analysis, Data curation. **Monsurat O. Jimoh:** Formal analysis, Methodology, Supervision, Validation, Visualization, Writing – review & editing. **Mabafokeng Masitha:** Writing – review & editing, Supervision, Methodology. **Samuel A. Iwarere:** Writing – review & editing, Visualization, Validation, Supervision, Methodology, Conceptualization. **Michael O. Daramola:** Writing – review & editing, Validation, Supervision, Resources, Project administration, Funding acquisition, Conceptualization.

Declaration of competing interest

The authors declare that they have no known competing financial interests or personal relationships that could have appeared to influence the work reported in this manuscript.

Acknowledgments

The author would like to appreciate Dr. Isbe van der Westhuizen, the lab manager, for assistance with analyses and characterization. The financial support of the MasterCard foundation scholars program at the University of Pretoria cannot be understated. Finally, the author acknowledges the support of the Sustainable Energy and Environment research group in the Department of Chemical Engineering at the University of Pretoria.

References

Adebayo, G.B., Jamiu, W., Okoro, H.K., Okeola, F.O., Adesina, A.K., Feyisetan, O.A, 2019. Kinetics, thermodynamics and isothermal modelling of liquid phase adsorption of methylene blue onto moringa pod husk activated carbon. South African J. Chem. 72. https://doi.org/10.17159/0379-4350/2019/v72a34.

Agarwal, S., Tyagi, I., Gupta, V.K., Bagheri, A.R., Ghaedi, M., Asfaram, A., Hajati, S., Bazrafshan, A.A., 2016. Rapid adsorption of ternary dye pollutants onto copper (i) oxide nanoparticle loaded on activated carbon: experimental optimization via response surface methodology. J. Environ. Chem. Eng. 4. https://doi.org/10.1016/j.jece.2016.03.002.

Aghababaei, A., Azargohar, R., Dalai, A.K., Soltan, J., Niu, C.H., 2021. Effective adsorption of carbamazepine from water by adsorbents developed from flax shives and oat hulls: key factors and characterization. Ind. Crops. Prod. 170. https://doi.org/10.1016/j.indcrop.2021.113721.

Aghababaei, A., Borugadda, V.B., Dalai, A., Niu, C.H., 2023. An investigation on adsorption of carbamazepine with adsorbents developed from flax shives: kinetics, mechanisms, and desorption. Chem. Eng. Res. Design 189. https://doi.org/10.1016/j.cherd.2022.11.008.

Agilandeswari, P., Venkateshbabu, S., Sarojini, G., Rajasimman, M., 2024. Sustainable development and analysis of a novel bio-derived (biochar) nanocomposite for the remediation of carbamazepine from aqueous solution. Chemosphere 347. https://doi.org/10.1016/j.chemosphere.2023.140696.

Ali, M.E.M., Abdelsalam, H., Amma, N.S., Ibrahim, H.S., 2018. Response surface methodology for optimization of the adsorption capability of ball-milled pomegranate peel for different pollutants. J. Mol. Liq. https://doi.org/10.1016/j.molliq.2017.12.025.

Álvarez-Torrellas, S., Peres, J.A., Gil-Álvarez, V., Ovejero, G., García, J., 2017. Effective adsorption of non-biodegradable pharmaceuticals from hospital wastewater with different carbon materials. Chem. Eng. J. 320. https://doi.org/10.1016/j.cej.2017.03.077.

Alver, A., Yılmaz, B.A., Bilican, B.K., Ba¸stürk, E., Kaya, M., I¸sık, M., 2024. Carbamazepine adsorption onto giant macroporous silica and adaptive neuro-fuzzy inference system modeling. Arab. J. Sci. Eng. 49. https://doi.org/10.1007/s13369-024-09032-3.

Araujo, L.A., Bezerra, C.O., Cusioli, L.F., Silva, M.F., Nishi, L., Gomes, R.G., Bergamasco, R., 2018. Moringa oleifera biomass residue for the removal of pharmaceuticals from water. J. Environ. Chem. Eng. 6. https://doi.org/10.1016/j.jece.2018.11.016.

Archer, E., Petrie, B., Kasprzyk-Hordern, B., Wolfaardt, G.M., 2017. The fate of pharmaceuticals and personal care products (ppcps), endocrine disrupting contaminants (edcs), metabolites and illicit drugs in a wwtw and environmental waters. Chemosphere 174. https://doi.org/10.1016/j.chemosphere.2017.01.10.

Ayawei, N., Ebelegi, A.N., Wankasi, D., 2017. Modelling and interpretation of adsorption isotherms. J. Chem. 2017. https://doi.org/10.1155/2017/3039817.

Baghdadi, M., Ghaffari, E., Aminzadeh, B., 2016. Removal of carbamazepine from municipal wastewater effluent using optimally synthesized magnetic activated carbon: adsorption and sedimentation kinetic studies. J. Environ. Chem. Eng. 4. https://doi.org/10.1016/j.jece.2016.06.034.

Bartlet-Hunt, S., Snow, D., Damon, T., Shockley, J., Hoagland, K., 2009. The occurrence of illicit and therapeutic pharmaceuticals in wastewater effluent and surface waters in nebraska. Environ. Pollut. 157. https://doi.org/10.1016/j.envpol.2008.11.025.

Bhattacharya, S., Banerjee, P., Das, P., Bhowal, A., Majumder, S.K., Ghosh, P., 2020. Removal of aqueous carbamazepine using graphene oxide nanoplatelets: process modelling and optimization. Sustain. Environ. Res. 30. https://doi.org/10.1186/s42834-020-00062-8.

Branchet, P., Castro, N.A., Fenet, H., Gomez, E., Courant, F., Sebag, D., Gardon, J., Jourdan, C., Ngatcha, B.N., Kengne, I., et al., 2019. Anthropic impacts on sub-saharan urban water resources through their pharmaceutical contamination (yaoundé, center region, cameroon). Sci. Total Environ. 660. https://doi.org/10.1016/j.scitotenv.2018.12.256.

Cevallos-Mendoza, J., Amorim, C.G., Rodríguez-Díaz, J.M., Conceição, M.d., Montenegro, B.S.M., 2022. Removal of contaminants from water by membrane filtration: a review. Membranes. (Basel) 12. https://doi.org/10.3390/membranes12060570.

Chen, D., Xie, S., Chen, C., Quan, H., Hua, L., Luo, X., Guo, L., 2017a. Activated biochar derived from pomelo peel as a high-capacity sorbent for removal of carbamazepine from aqueous solution. RSC. Adv. 7. https://doi.org/10.1039/c7ra10805b.

Chen, G., Dong, W., Wang, H., Zhao, Z., Wang, F., Wang, F., Nieto-Delgado, C., 2022. Carbamazepine degradation by visible-light-driven photocatalyst ag3po4/go: mechanism and pathway. Environ. Sci. Ecotoxicol. 9. https://doi.org/10.1016/j.ese.2021.100143.

Chen, J., Zhang, D., Zhang, H., Ghosh, S., Pan, B., 2017b. Fast and slow adsorption of carbamazepine on biochar as affected by carbon structure and mineral composition. Sci. Total Environ. 579. https://doi.org/10.1016/j.scitotenv.2016.11.052.

Chen, S., 2020. Catalytic Graphitization of Biochar to Produce Graphitic Carbon Materials. KTH Royal Institute of Technology.

Cleuvers, M., 2003. Aquatic ecotoxicity of pharmaceuticals including the assessment of combination effects. Toxicol. Lett. 142. https://doi.org/10.1016/S0378-4274(03)00068-7.

Coldebella, P.F., Fagundes-Klen, M.R., Letícia Nishi, K.C.V., Cavalcanti, E.B., Santos, O.A.A.d., Bergamasco, R., 2016. Potential effect of chemical and thermal treatment on the kinetics, equilibrium, and thermodynamic studies for atrazine biosorption by the moringa oleifera pods. Can. J. Chem. Eng. 95. https://doi.org/10.1002/cjce.22756.

Couto, C.F., Lange, L.C., Amaral, M.C.S., 2019. Occurrence, fate and removal of pharmaceutically active compounds (phacs) in water and wastewater treatment plants - a review. J. Water. Process. Eng. 32. https://doi.org/10.1016/j.jwpe.2019.100927.

Cunningham, V.L., Perino, C., D'Aco, V.J., Hartmann, A., Bechter, R., 2010. Human health risk assessment of carbamazepine in surface waters of north america and europe. Regulat. Toxicol. Pharmacol. 56. https://doi.org/10.1016/j.yrtph.2009.10.006.

de Souza, H.K.S., Klen, M.R.F., Wernke, G., Mantovani, D., Nishi, L., Shimabuku-Biadola, Q.L., Vieira, M.F., Bergamasco, R., Vieira, A.M.S., 2019. Improvement of adsorption conditions of different parts of moringa oleifera on the perception of diuron removal from contaminated waters. Desalinat. Water Treatment 171. https://doi.org/10.5004/dwt.2019.24770.

Décima, M.A., Marzeddu, S., Barchiesi, M., Marcantonio, C.D., Chiavola, A., Boni, M.R., 2021. A review on the removal of carbamazepine from aqueous solution by using activated carbon and biochar. Sustainability. 13. https://doi.org/10.3390/su132111760.

Domingues, R.R., Trugilho, P.F., Silva, C.A., de Melo, I.C.N.A., A, L.C., Magriotis, Z.M., Sanchez-Monedero, M.A, 2017a. Properties of biochar derived from wood and high-nutrient biomasses with the aim of agronomic and environmental benefits. PLoS. One 12. https://doi.org/10.1371/journal.pone.0176884.

Domingues, R.R., Trugilho, P.F., Silva, C.A., Melo, I.C.N.A.d., Melo, L.C.A., Magriotis, Z.M., Sánchez-Monedero, M.A., 2017b. Properties of biochar derived from wood and high-nutrient biomasses with the aim of agronomic and environmental benefits. PLoS. One. https://doi.org/10.1371/journal.pone.0176884.

Elgarahy, A.M., Elwakeel, K.Z., Mohammad, S.H., Elshoubaky, G.A., 2021. A critical review of biosorption of dyes, heavy metals and metalloids from wastewater as an

efficient and green process. Clean. Eng. Technol. 4. https://doi.org/10.1016/j.clet.2021.100209.
Ellerbrock, R.H., Gerke, H.H., 2021. Ftir spectral band shifts explained by om–cation interactions. J. Plant Nutrit. Soil Sci. 184. https://doi.org/10.1002/jpln.202100056.
Farrokhzadeh, H., Taheri, E., Ebrahimi, A., Fatehizadeh, A., Dastjerdi, M.V., Bina, B., 2013. Effectiveness of moringa oleifera powder in removal of heavy metals from aqueous solutions. Fresen. Environ. Bullet. 22.
Gamero-Salinas, J., López-Fidalgo, J., 2025. Response surface methodology using desirability functions for multiobjective optimization to minimize indoor overheating hours and maximize useful daylight illuminance. Sci. Rep. 15. https://doi.org/10.1038/s41598-025-96376-x.
García-fayos, B., Arnal, J.M., Piris, J., Sancho, M., 2016. Valorization of moringa oleifera seed husk as biosorbent: isotherm and kinetics studies to remove cadmium and copper from aqueous solutions. Desalin. Water Treat 57. https://doi.org/10.1080/19443994.2016.1180473.
Gupta, A., Sharma, V., Sharma, K., Kumar, V., Choudhary, S., Mankotia, P., Kumar, B., Mishra, H., Moulick, A., Ekielski, A., Mishra, P.K., 2021. A review of adsorbents for heavy metal decontamination: growing approach to wastewater treatment. Materials. (Basel) 14. https://doi.org/10.3390/ma14164702.
Jabar, J.M., Odusote, Y.A., Alabi, K.A., Ahmed, I.B., 2020. Kinetics and mechanisms of congo-red dye removal from aqueous solution using activated moringa oleifera seed coat as adsorbent. Appl. Water. Sci. 10. https://doi.org/10.1007/s13201-020-01221-3.
Jiang, H., Shao, J.a., Hu, Q., Zhu, Y., Cheng, W., Zhang, J., Fan, T., Yu, J., Yang, H., Zhang, X., Chen, H., 2024. Carbon black production characteristics and mechanisms from pyrolysis of rubbers. Fuel Process. Technol. 253. https://doi.org/10.1016/j.fuproc.2023.108011.
Jönsson, L.J., Martín, C., 2016. Pretreatment of lignocellulose: formation of inhibitory by-products and strategies for minimizing their effects. Bioresour. Technol. 199. https://doi.org/10.1016/j.biortech.2015.10.009.
Jos, A., Repetto, G., Rios, J.C., Hazen, M.J., Molero, M.L., Peso, A.d., Salguero, M., Fernández-Freire, P., Pérez-Martín, J.M., Cameán, A., 2003. Ecotoxicological evaluation of carbamazepine using six different model systems with eighteen endpoints. *Toxicol.* Vitro 17. https://doi.org/10.1016/S0887-2333(03)00119-X.
Keereerak, A., Chinpa, W., 2020. A potential biosorbent from moringa oleifera pod husk for crystal violet adsorption: kinetics, isotherms, thermodynamic and desorption studies. Sci. Asia 46. https://doi.org/10.2306/scienceasia1513-1874.2020.034.
Ketharani, J., Hansima, M.A.C.K., Indika, S., Samarajeewa, D.R., Makehelwala, M., Jinadasa, K.B.S.N., Weragoda, S.K., Rathnayake, R.M.L.D., Nanayakkara, K.G.N., Wei, Y., et al., 2022. A comparative study of community reverse osmosis and nanofiltration systems for total hardness removal in groundwater. Groundw. Sustain. Dev. 18. https://doi.org/10.1016/j.gsd.2022.100800.
Kritikaki, A., Karmali, V., Vathi, D., Bartzas, G., Komnitsas, K., 2025. Advanced characterization of biochars produced from three different organic-based feedstocks and their potential applications. Circ. Econ. Sustain. 1. https://doi.org/10.1007/s43615-025-00580-w.
Largitte, L., Pasquier, R., 2016. A review of the kinetics adsorption models and their application to the adsorption of lead by an activated carbon. Chem. Eng. Res. Design 109. https://doi.org/10.1016/j.cherd.2016.02.006.
Lee, S.M., Lee, J.H., Nam, G., Kim, S.H., Kim, J., Roh, J.S., 2019. Surface shape and pore size change in carbon blacks isothermally oxidized in air atmosphere according to burn-off ratio. Carbon letters 29. https://doi.org/10.1007/s42823-019-00061-9.
LibreTexts Chemistry, 2024. Infrared Spectroscopy Absorption Table. https://chem.libretexts.org/Ancillary_Materials/Reference/Reference_Tables/Spectroscopic_Reference_Tables/Infrared_Spectroscopy_Absorption_Table.
Liu, Z., Zhou, X., Chen, X., Dai, C., Zhang, J., Zhang, Y., 2013. Biosorption of clofibric acid and carbamazepine in aqueous solution by agricultural waste rice straw. J. Environ. Sci. 25. https://doi.org/10.1016/S1001-0742(12)60324-6.
Lopes, C.A., Roledo, C., Reis, A.G.d., 2022. Moringa oleifera seed husks for methylene blue dye adsorption: kinetic, equilibrium, and thermodynamic analyses. Ambiente Água - An Interdisciplin. J. Appl. Sci. 17. https://doi.org/10.4136/ambi-agua.2812.
Mansouri, F., Chouchene, K., Roche, N., Ksibi, M., 2021. Removal of pharmaceuticals from water by adsorption and advanced oxidation processes: state of the art and trends. Appl. Sci. 11. https://doi.org/10.3390/app11146659.
Marinković, V., 2021. Some applications of a novel desirability function in simultaneous optimization of multiple responses. FME Transac. 49. https://doi.org/10.5937/fme2103534M.
Marques, D., Mota, S., Freitas, M.M., Silva, P.C., 2022. Ciprofloxacin and carbamazepine adsorption on activated carbons produced from leather residues. Desalin. Water Treatment 260. https://doi.org/10.5004/dwt.2022.28549.
Naghdi, M., Taheran, M., Pulicharla, R., Rouissi, T., Brar, S.K., Verma, M., 2019. Pine-wood derived nanobiochar for removal of carbamazepine from aqueous media: adsorption behavior and influential parameters. Arab. J. Chem. 12. https://doi.org/10.1016/j.arabjc.2016.12.025.
Nezhadali, A., Koushali, S.E., Divsar, F., 2022. Synthesis of polypyrrole-chitosan magnetic nanocomposite for the removal of carbamazepine from wastewater: adsorption isotherm and kinetic study. J. Environ. Chem. Eng. 9. https://doi.org/10.1016/j.jece.2021.105648.
Odendaal, C., Seaman, M.T., Kemp, G., Patterton, H.E., Patterton, H.-G., 2015. An lc-ms/ms based survey of contaminants of emerging concern in drinking water in south africa. Contamin. Emerg. Concern Drinking Water 111. https://doi.org/10.17159/sajs.2015/20140401.
Pareek, A., Pant, M., Gupta, M.M., Kashania, P., Ratan, Y., Jain, V., Pareek, A., A. Chuturgoon, A., 2023. Moringa oleifera: an updated comprehensive review of its pharmacological activities, ethnomedicinal, phytopharmaceutical formulation, clinical, phytochemical, and toxicological aspects. Int. J. Mol. Sci. 24. https://doi.org/10.3390/ijms24032098.
Pasieczna-Patkowska, S., Cichy, M., Flieger, J., 2025. Application of fourier transform infrared (ftir) spectroscopy in characterization of green synthesized nanoparticles. Molecules. 30. https://doi.org/10.3390/molecules30030684.
Puga, A., Soares, C., Álamo, A.C.d., Pariente, M.I., Molina, R., Martínez, F., Sanromán, M. A., Pazos, M.M., Delerue-Matos, C., 2024. Efficient carbamazepine removal from wastewater using a continuous three-dimensional electro-fenton system at natural ph. J. Water. Process. Eng. 64. https://doi.org/10.1016/j.jwpe.2024.105690.
Qiang, L., Cheng, J., Yi, J., Rotchell, J.M., Zhu, X., Zhou, J., 2016. Environmental concentration of carbamazepine accelerates fish embryonic development and disturbs larvae behavior. Ecotoxicology. 25. https://doi.org/10.1007/s10646-016-1694-y.
Quesada, H.B., Cusioli, L.F., Bezerra, C.d.O., Baptista, A.T., Nishi, L., Gomes, R.G., Bergamasco, R., 2019. Acetaminophen adsorption using a low-cost adsorbent prepared from modified residues of moringa oleifera lam. Seed husks. J. Chem. Technol. Biotechnol. 94.
Radjenović, J., Petrović, M., Ventura, F., Barcelo', D., 2008. Rejection of pharmaceuticals in nanofiltration and reverse osmosis membrane drinking water treatment. Water. Res. 42. https://doi.org/10.1016/j.watres.2008.05.020.
Regti, A., Laamari, R., Salah-Eddine, S., Mohammadine, E.H., 2017. Use of response factorial design for process optimization of basic dye adsorption onto activated carbon derived from persea species. Microchem. J. 130. https://doi.org/10.1016/j.microc.2016.08.012.
Rossi, L., Villabrille, P.I., Marino, D.J., Rosso, J.A., Caregnato, P., 2023. Degradation of carbamazepine in surface water: performance of pd-modified tio2 and ce-modified zno as photocatalysts. Environ. Sci. Pollut. Res. 30. https://doi.org/10.1007/s11356-023-30531-7.
Serafin, J., Dziejarski, B., 2023. Application of isotherms models and error functions in activated carbon co2 sorption processes. Micropor. Mesopor. Mater. 354. https://doi.org/10.1016/j.micromeso.2023.112513.
Shin, J., Lee, Y.-G., Lee, S.-H., Kim, S., Ochir, D., Park, Y., Kim, J., Chon, K., 2020. Single and competitive adsorptions of micropollutants using pristine and alkali-modified biochars from spent coffee grounds. J. Hazard. Mater. 400. https://doi.org/10.1016/j.jhazmat.2020.123102.
Sing, K.S.W., Everett, D.H., Haul, R.A.W., Moscou, L., Pierotti, R.A., Rouquerol, J., Siemieniewska, T., 1985. Reporting physisorption data for gas/solid systems with special reference to the determination of surface area and porosity. Pure Appl. Chem. 57.
Starbuck, C. (2023) The fundamentals of people analyticswith applications in r (Springer). https://doi.org/10.1007/978-3-031-28674-2.
Tan, X., Liu, Y., Zeng, G., Wang, X., Hu, X., Gu, Y., Yang, Z., 2015. Application of biochar for the removal of pollutants from aqueous solutions. Chemosphere 125. https://doi.org/10.1016/j.chemosphere.2014.12.058.
To, M.-H., Hadi, P., Hui, C.-W., Lin, C.S.K., AI-Ansari, T., Saleem, J., Parthasarathy, P., McKay, G., 2019. Waste biomass gasification char derived activated carbon for pharmaceutical carbamazepine removal from water. Resour. Environ. Informat. Eng. 1. https://doi.org/10.25082/REIE.2019.01.005.
Tran, N.H., Li, J., Hu, J., Ong, S.L., 2014. Occurrence and suitability of pharmaceuticals and personal care products as molecular markers for raw wastewater contamination in surface water and groundwater. Environ. Sci. Pollut. Res. 21. https://doi.org/10.1007/s11356-013-2428-9.
Tran, N.H., Reinhard, M., Gin, K.Y.-H, 2018. Occurrence and fate of emerging contaminants in municipal wastewater treatment plants from different geographical regions-a review. Water. Res. 133. https://doi.org/10.1016/j.watres.2017.12.029.
Viegas, R.M.A., Melo, M.L., Lima, L.C.B., Garcia, R.R.P., Filho, E.C.S., Osajima, J.A., Chiavone-Filho, O., 2024. Carbamazepine adsorption with a series of organoclays: removal and toxicity analyses. Appl. Water. Sci. 14. https://doi.org/10.1007/s13201-024-02198-z.
Wang, Y., Wang, S.-l., Xie, T., Cao, J., 2020. Activated carbon derived from waste tangerine seed for the high performance adsorption of carbamate pesticides from water and plant. Bioresour. Technol. 316.
Wijitkosum, S., Jiwnok, P., 2019. Elemental composition of biochar obtained from agricultural waste for soil amendment and carbon sequestration. Appl. Sci. 9. https://doi.org/10.3390/app9193980.
Wu, M., Xiang, J., Que, C., Chen, F., Xu, G., 2015. Occurrence and fate of psychiatric pharmaceuticals in the urban water system of shanghai, china. Chemosphere 138. https://doi.org/10.1016/j.chemosphere.2015.07.002.
Yaashikaa, P.R., Kumar, P.S., Saravanan, A., Vo, D.-V.N., 2021. Advances in biosorbents for removal of environmental pollutants: a review on pretreatment, removal mechanism and future outlook. J. Hazard. Mater. 420. https://doi.org/10.1016/j.jhazmat.2021.126596.
Yan, S., Chen, R., Wang, M., Zha, J., 2021. Carbamazepine at environmentally relevant concentrations caused DNA damage and apoptosis in the liver of chinese rare minnows (gobiocypris rarus) by the ras/raf/erk/p53 signaling pathway. Environ. Pollut. 270. https://doi.org/10.1016/j.envpol.2020.116245.
Zeghioud, H., Fryda, L., Mahieu, A., Visser, R., Kane, A., 2022. Potential of flax shives and beech wood-derived biochar in methylene blue and carbamazepine removal from aqueous solutions. Materials 15. https://doi.org/10.3390/ma15082824.
Zhang, Y., Geißen, S.-U., Gal, C., 2008. Carbamazepine and diclofenac: removal in wastewater treatment plants and occurrence in water bodies. Chemosphere. https://doi.org/10.1016/j.chemosphere.2008.07.086.
Zhong, H., Zhu, G., Wang, Z., Liu, X., Zhang, H., Qiu, Y., Yin, D., Zhu, Z., 2025. Efficient adsorption removal of carbamazepine from water by dual-activator modified hydrochar. Sep. Purif. Technol. 353. https://doi.org/10.1016/j.seppur.2024.128287.